



Experimental and Computational Design of Highly Active Ce–ZrO₂–GO Photocatalyst for Eosin Yellow Dye Degradation: The Role of Interface and Ce³⁺ Ion

Samuel Osei-Bonsu Oppong¹ · Francis Opoku¹ · William Wilson Anku¹ · Ephraim Muriithi Kiarri¹ · Penny Poomani Govender¹

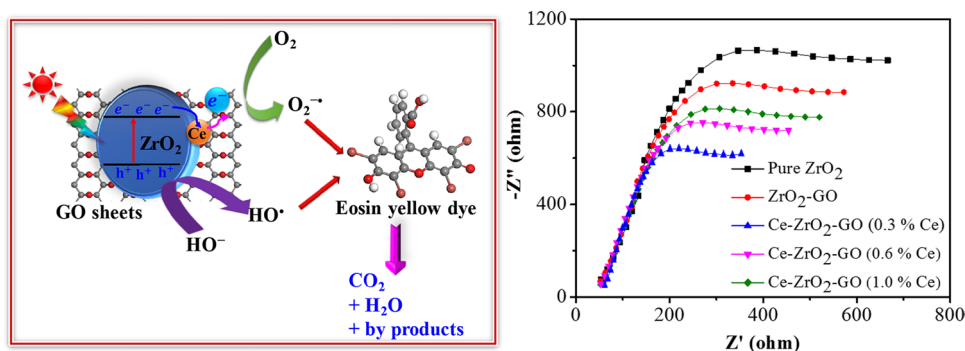
Received: 26 October 2018 / Accepted: 4 March 2019 / Published online: 15 March 2019
© Springer Science+Business Media, LLC, part of Springer Nature 2019

Abstract

As future photocatalyst require high activity and structural stability, the demand for high-performance photocatalyst that increases photocatalytic conversion efficiency is of significant interest. In this study, Ce–ZrO₂–GO nanocomposite was fabricated by a co-precipitation technique and used for the photocatalytic degradation of eosin yellow (EY) dye under visible light irradiation. A hybrid DFT calculation was employed to analyse the electronic properties and the underlying mechanism of the observed photoactivity. The as-prepared Ce–ZrO₂–GO (0.3% Ce) nanocomposite showed enhanced photodegradation of EY dye, which was about 15.98-fold higher than pure ZrO₂. The enhanced performance of Ce–ZrO₂–GO nanocomposite for EY dye degradation is due to the synergistic effect between the GO sheets and Ce–ZrO₂. From the computational study, Ce ion could act as an electron mediator to capture the photoinduced electrons from ZrO₂ to restrain the recombination rate of charge carriers. Testing with different scavengers showed that hydroxyl radicals play a major contribution to the degradation of EY dye with a pseudo first-order reaction kinetics. Total Organic Carbon analysis showed 76% mineralisation of EY dye over Ce–ZrO₂–GO (0.3% Ce) nanocomposite, which is photostable and its efficiency remained almost the same after five cycles without any photocorrosion. The present study could offer an alternative approach to develop highly efficient photocatalysts for organic pollutant degradation using metal ion as a mediator to enhance charge migration, activity and structural stability of the nanocomposite.

Graphical Abstract

A series of Ce–ZrO₂–GO nanocomposite were employed as a photocatalytic to degrade eosin yellow dye from wastewater. The present study offers an alternative approach to develop highly efficient photocatalysts for organic pollutant degradation using Ce ion as a mediator to enhance charge migration, activity and structural stability of the nanocomposite.



Keywords ZrO₂ · Eosin yellow · Hybrid density functional theory · Co-precipitation technique · Photodegradation

1 Introduction

Heavy metals and industrial organic dyes are regarded as the most vital sources of water pollution [1]. The discharge of dye residues by the dye manufacturing and textile industries is highly carcinogenic and toxic to human health [2]. Since dyes are discharged in high concentration, their removal by the conventional techniques, such as adsorption on activated carbon, biological oxidation, coagulation and filtration is ineffective and expensive [3]. Therefore, it is more significant to design an economical, simple and eco-friendly method that can remove toxic dyes from contaminated water resources [4]. Environmental remediation based on visible light induced semiconductor photocatalysis has been shown as an efficient and cost-effective technique for removing dyes from wastewater [5–8].

Up to now, most of the materials used in photocatalysis are semiconductors, such as ZrO_2 , ZnO and TiO_2 . Environmental friendly zirconia (ZrO_2) is among one of the important metal oxides with cost-effective, high chemical inertness, biocompatible, less toxicity, high thermal stability and electrochemical nature [2, 9]. The surface of ZrO_2 has both basic and acidic properties, and therefore, display reduction and oxidation properties, as well as photoactivity [10]. As a typical functional and structural material, ZrO_2 has been extensively used in solid oxide fuel cells [11], adsorbents [12], catalyst supports [13] and photocatalysis [14]. Despite the good chemical stability and activity of ZrO_2 , its photoactivity was restricted due to its large bandgap energy (5–5.8 eV) and faster rate of electron–hole pairs recombination [15]. In an attempt to extend its visible light photoactivity and minimise the electron–hole pairs recombination rate, several approaches such as elemental doping, dye sensitisation, hybridising with visible light bandgap semiconductors or carbon materials and others have been used [16].

The design of heterojunction materials has been used as an effective strategy in water treatment to decrease the electron–hole pairs recombination rate and extend the visible light absorption edge [17]. Up to now, graphene oxide (GO) with a fascinating sp^2 carbon arrangement in the two-dimensional carbon framework has attracted much attention because of its high Young's modulus, large surface area, high electron conductivity and charge carrier mobility [18]. Again, studies have shown that GO is an exceptional absorber of organic pollutants because of its π – π loading interaction and aromatic nature [19]. Based on the aforementioned properties, graphene oxide–metal oxide nanocomposites with excellent photochemical properties and structural morphology have been used in water treatment *via* the elimination of heavy metals and degradation of toxic organic contaminants [20]. The decoration of

ZrO_2 on GO sheets as a photocatalyst and fuel cell transistor has been reported [21], where ZrO_2 nanoparticles showed endowed properties when coupled with GO sheets [22].

Besides the design of heterojunction nanomaterials, doping of lanthanide ions has been demonstrated to further promote the separation of charge carriers and visible light performance [23]. The presence of lanthanide ions also promotes the semiconductor spectra to shift from a lower energy range leading to the enhancement in their photoactivity [24]. Due to the unique spectral characteristics and 4f electronic configuration, lanthanide ions are ideal dopants for modifying the surface adsorption, optical properties, electronic and crystal structures of several semiconductors [25]. Moreover, the introduction of lanthanide ions could form complexes with several organic molecules by concentrating the pollutants on the photocatalyst surface and hence, promote the photocatalytic reactivity [26]. As one of the lanthanide ions, several studies have shown that the use of cerium ion as dopant leads to excellent photoactivity [27]. Because of the higher separation of charge carriers, and the adsorption equilibrium constant, Ce^{3+} – TiO_2 showed an enhanced photoactivity towards 2-mercaptobenzothiazole degradation. Also, Xie and Yuan [28] reported that Ce^{4+} – TiO_2 exhibited enhanced photoactivity towards X-3B degradation.

Though studies on the visible light performance of Ce – ZrO_2 and ZrO_2 –GO nanocomposite have been reported, studies on Ce – ZrO_2 –GO as a visible light material is unknown. Therefore, this study was aimed to prepare several hybrid visible-light-driven Ce – ZrO_2 –GO (0.3, 0.6 and 1.00% Ce) nanocomposites using a co-precipitation technique and examine its photocatalytic performance *via* the photodegradation of eosin yellow (EY) dye under solar light irradiation. In the Ce – ZrO_2 –GO nanocomposite, the introduction of Ce^{3+} as dopants can create energy levels just below the conduction band (CB) of ZrO_2 , thereby promoting its visible light performance, while the introduction of GO sheets with ZrO_2 can promote the lifetime of the charge carriers by forming a heterojunction. In this study, the transfer pathway of charge carriers, electronic and structural properties of hybrid Ce – ZrO_2 –GO nanocomposites were theoretically investigated to assist in explaining the origin of the improved photocatalytic activity and stability. This study could offer novel insights for a better understanding of the role of Ce^{3+} ions and GO sheets for the removal of organic pollutants from wastewater.

2 Materials and Methods

2.1 Materials and Reagents

All the chemicals obtained from Sigma–Aldrich was used without further purification.

2.2 Fabrication of GO

The GO was prepared following our earlier report [29] and employed the modified Hummers method [30].

2.3 Preparation of Ce–ZrO₂–GO Photocatalyst

A literature procedure [31], which was adopted for the synthesis of the composites, involved the dispersion and sonication of 9.81 g of Zr(NO₃)₂·6H₂O and a specific quantity of Ce(NO₃)₃·6H₂O (0.04527, 0.09054 and 0.1505 g) in 50 mL of deionised water to obtain 0.3, 0.6 and 1.0% of Ce-doped ZrO₂ nanocomposites. The mixtures were stirred magnetically for an hour. After the addition of 0.5% of GO, stirring was continued at 50 °C for a further 2 h. A solution of 3M KOH was then added dropwise under stirring conditions into the Ce–ZrO₂–GO mixture until a precipitate was formed at a pH of 10. The obtained nanocomposites [Ce–ZrO₂–GO (0.3, 0.6 and 1.0% Ce)] were rinsed with both water and ethanol using a centrifuge to get rid of any contaminants. Finally, the isolated nanocomposites were dried overnight at 90 °C and calcined at 300 °C for 3 h. Pure ZrO₂ and ZrO₂–GO nanocomposite were also fabricated by the same technique, but without the addition of either Ce(NO₃)₃·6H₂O or both GO and Ce(NO₃)₃·6H₂O, respectively.

2.4 Characterisation

Perkin Elmer Raman microscope (Raman Micro 200) and Perkin Elmer FTIR spectroscopy (Spectrum 100) were used to measure the Raman and FTIR spectrum, respectively. The microstructure, crystal phase and morphology of the fabricated samples were characterised by Philip's X-ray diffractometer at 30 mA and 40 kV. The surface morphology of the photocatalyst was evaluated by the scanning electron microscopy on TESCAN (Vega 3XMU), while transmission electron spectroscopy was used to measure the size and internal morphology of the prepared samples (JEOL, JEM-2100F). The Shimadzu UV-2540 Spectrophotometer with BaSO₄ as a reflectance standard was used to evaluate the optical properties.

2.5 Photocatalysis Study

The photocatalytic degradation reaction of the as-synthesised nanocomposite was examined using a Full-Spectrum Solar Simulator (Newport, Model: 9600). The solar simulator was equipped with 150 W ozone free xenon lamp, where a collimated beam of 33 mm diameter, which is an equivalent of 1.3 suns was produced. The EY dye concentration in the sample of 5 mL suspension was evaluated by a Shimadzu UV-2450 spectrophotometer at a λ of 516 nm. In this process, 100 mg of the photocatalyst was suspended in

an aqueous solution of 20 mg/L of IC dye and then magnetically stirred in the dark, prior to irradiation, for 1 h and at 25 °C in a quartz beaker (150 mL) and this was carried out to create an adsorption equilibrium of IC dye with the semiconductor photocatalyst. After the adsorption equilibrium, the light sources were switched on for photodegradation of IC dye at 30 min intervals by the various photocatalysts and aliquots (5 mL) was withdrawn from the solution using a disposal syringe containing filtered membrane of 4 μ m for a period of 210 min.

2.6 Density Functional Theory Calculations

The electronic and structural properties were performed using a plane-wave DFT calculation implemented in the CASTEP code [32] of the Materials Studio 2016 [33]. The geometry optimisation was carried out using the conjugate gradient method [34] and the generalized gradient approximation (GGA) with the Perdew–Burke–Ernzerhof (PBE) functional [35] for the exchange–correlation potential. The norm-conserving pseudopotential was used to describe the core–valence electrons interaction [36]. A valence states of Zr (4d² 5s²), O (2s² 2p⁴), C (2s² 2p²) and Ce (4f² 6s²) were considered to construct the potential. In this study, the electronic property was considered using the hybrid HSE06 functional [37], since the GGA–PBE functional normally underestimate the electronic properties of most photocatalysts [38]. The convergence criteria for maximum force and energy, and the cut-off was set at 0.01 eV/Å, 10^{−6} eV/atom and 500 eV, respectively. A large vacuum space of 20 Å was used to prevent the interactions between the periodic images. The Brillouin zone was described by the Monkhorst–Pack and a *k*-point grid of 2 × 2 × 1, 12 × 12 × 1 and 3 × 3 × 1 were used for the ZrO₂, GO sheet, ZrO₂–GO and Ce–ZrO₂–GO nanocomposites, respectively [39].

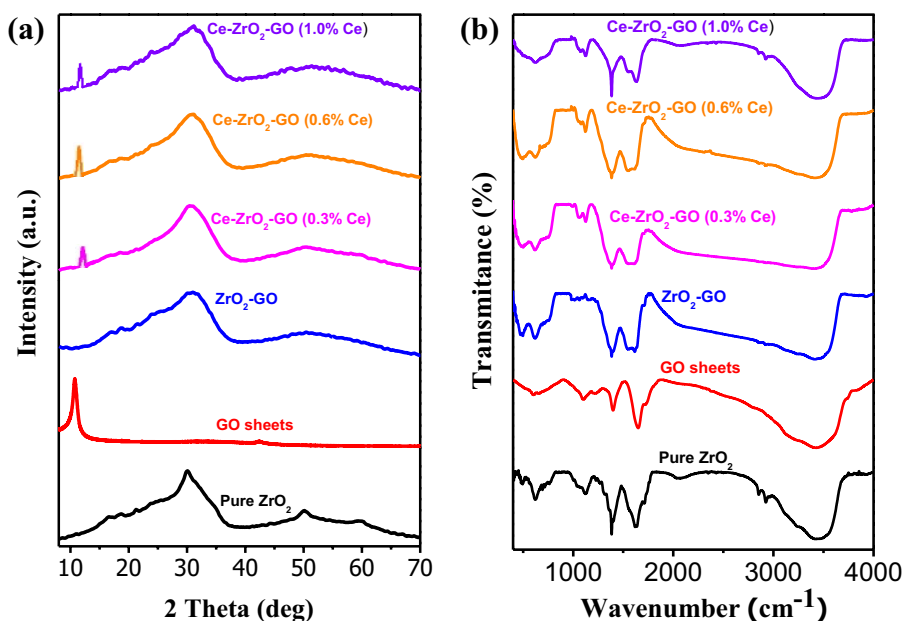
3 Results and Discussion

3.1 XRD Pattern Analysis

The crystal structures and phase purity of pure ZrO₂, GO sheets, ZrO₂–GO and Ce-doped ZrO₂–GO (with varied Ce concentrations) nanocomposites were evaluated using the X-ray diffractometer, and the corresponding X-ray diffraction pattern is given in Fig. 1a.

The characteristic XRD peaks of the tetragonal phase observed at 30.2°, 34.5°, 50.2° and 60.2° corresponding to the (101), (200), (220), and (311) reflection planes, respectively [40]. However, the diffraction peaks corresponding to 16.4°, 24.5°, 28.1° and 32.7° indexed to Miller indices of (011), (110), (111) and (110), respectively, agreed with the monoclinic phase of ZrO₂ (JCPDS No. 89-7710). The broad

Fig. 1 **a** XRD pattern and **b** FTIR spectra of pure ZrO_2 , GO sheets, ZrO_2 -GO and Ce-ZrO_2 -GO (with variable concentrations of Ce) nanocomposites



XRD pattern obtained for ZrO_2 nanoparticles was due to the small crystallite size of the chemically precipitated ZrO_2 [41], as well as the presence of tetragonal and monoclinic crystal structure [42]. The GO sheets showed a sharp diffraction peak around $2\theta = 10.72^\circ$ with a 0.77 nm interlayer distance, which corresponds to the (002) plane [43]. Due to the low concentration of GO in the nanocomposites, a low-intensity diffraction peak was observed for GO sheets in ZrO_2 -GO nanocomposite and this was in agreement with earlier studies on XRD characterisation of GO-based nanocomposites [44]. No peaks relating to Ce_2O_3 were observed in the Ce-ZrO_2 -GO nanocomposite. This revealed that Ce remained as a dispersed phase on the ZrO_2 surface or substituted Zr in the lattice sites [45]. The higher ionic radius of Ce^{3+} (1.03 Å) than that of Zr^{4+} (0.72 Å) indicated that surface doping occurred on the ZrO_2 surface [45]. In the Ce-ZrO_2 -GO (with variable concentrations of Ce) nanocomposites, peaks corresponding to monoclinic ZrO_2 and GO sheets were identified, confirming the successful fabrication of the nanocomposites.

3.2 FTIR Analysis

The functional groups of ZrO_2 , GO sheets, ZrO_2 -GO and Ce-doped ZrO_2 -GO nanocomposite (with varied Ce concentrations) were determined by the FTIR analysis, as given in Fig. 1b. The peak observed at 3460 and 1635 cm^{-1} relates to hydroxyl stretching and bending vibration bands of the absorbed water and hydrated oxide surface [46], while the broad absorption band situated at 576 and 750 cm^{-1} were ascribed to the Zr-O vibration [46]. The broad and strong peak at 3416 cm^{-1} in GO sheets could be related to the O-H

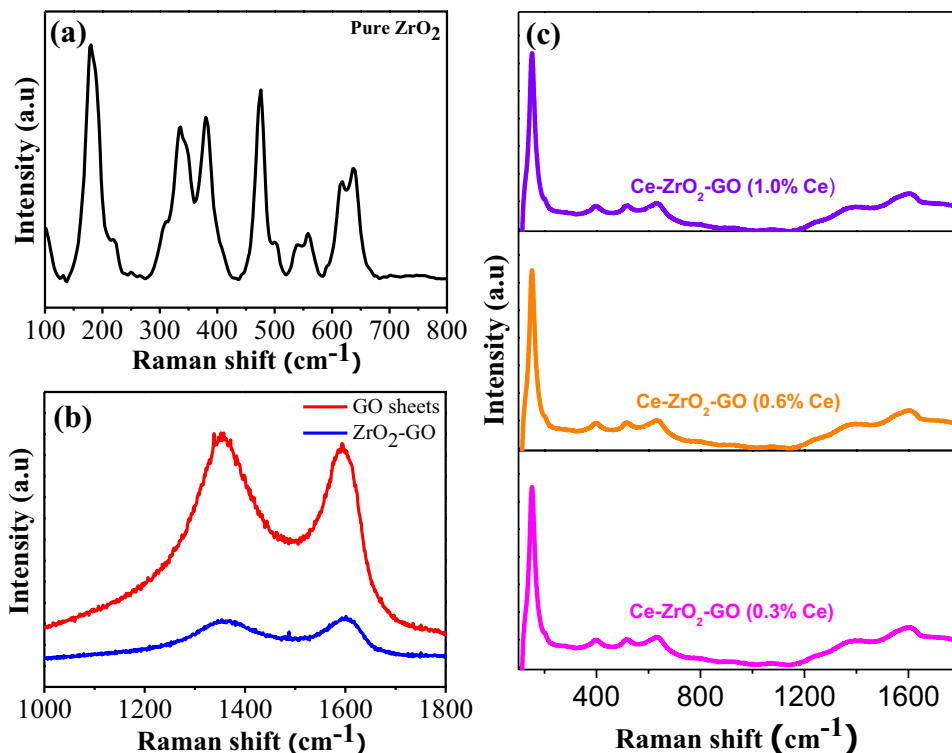
stretching vibration. The broad absorption peak around 1614 and 1732 cm^{-1} were due to C=O and carbonyl CO stretching, respectively, while the peaks at 1420 and 1055 cm^{-1} corresponded to the carboxyl OH stretching and C-O epoxy group at the edges of graphene oxide, respectively [43]. Due to the small concentration of GO sheets in the nanocomposite, the FTIR spectra of the ZrO_2 -GO nanocomposite showed bands corresponding to only ZrO_2 . However, the FTIR spectra of Ce-ZrO_2 -GO (with variable concentrations of Ce), which exhibit bands associated with ZrO_2 and GO, confirmed the successful fabrication of the nanocomposite.

3.3 Raman Studies

To check the different phases in the as-prepared nanocomposite samples, Raman spectra were plotted, and the results are given in Fig. 2.

Pure ZrO_2 and ZrO_2 -GO (Fig. 2a) showed peaks at 178, 334, 380, 476, 540, 558, 618 and 638 cm^{-1} and these pertained to the A_g , B_g , A_g , A_g , A_g , A_g and A_g modes of the monoclinic phase, respectively [45]. The GO and ZrO_2 -GO nanocomposite showed two distinct D (1366 cm^{-1}) and G (1599 cm^{-1}) Raman bands [47]. Raman spectra of Ce-ZrO_2 -GO nanocomposites showed peaks related to monoclinic ZrO_2 and GO sheets and this indicated that ZrO_2 and GO sheets were present in the nanocomposites, which were consistent with the XRD results. The D and G band of GO was due to the breathing mode of A_{1g} and E_{2g} mode of ordered sp^2 -bonded C atoms, respectively. The degree of disorder in GO was obtained by the ratio of the intensity of D-band to that of the G-band [48]. Based on the different reduction levels, the intensity I_D/I_G ratio is a measure of

Fig. 2 Raman spectra of **a** pure ZrO₂, **b** GO sheets and ZrO₂–GO and **c** the Ce–ZrO₂–GO nanocomposites



defect concentration in graphene sheets, where a smaller intensity of I_D/I_G ratio suggests fewer sp^3 defects/disorder and better average size of the in-plane graphitic crystallite sp^2 domains [49]. The I_D/I_G ratio of GO sheets (0.96) in the present study agreed with an earlier study (1.04) [50]. Also, ZrO₂–GO and Ce–ZrO₂–GO nanocomposites showed a slight decrease in the I_D/I_G ratio of 0.75 and 0.72, respectively, compared with GO sheets. This suggests a strong interaction in the nanocomposites.

3.4 SEM and TEM Analysis

The nanostructure, morphology and uniformity of the as-fabricated nanocomposites were determined using TEM and SEM analysis (Fig. 3).

Figure 3a–c shows the SEM image of ZrO₂, ZrO₂–GO and Ce–ZrO₂–GO nanocomposites. The SEM image revealed a distinct pebble-like particles of ZrO₂ nanoparticle, which was irregular in shape (Fig. 3a). The incorporation of GO aids ZrO₂ nanoparticle to disperse smoothly in ZrO₂–GO nanocomposite, where GO sheets were in the form of flakes. The separation between the agglomerated nanoparticles increased in the Ce–ZrO₂–GO nanocomposite. Figure 3e showed that the TEM image of GO appeared as a 2D transparent structure, which confirmed the 2D nanosheets of GO with micrometre-long wrinkles. Due to the interfacial interactions and heterogeneous nucleation, ZrO₂ nanocrystals were densely deposited on the wrinkled paper-like structure

of GO sheets (Fig. 3f). The nanomaterial composition is obtained by EDX analysis. The presence of Zr, Ce, O and C elements in the Ce–ZrO₂–GO nanocomposite was confirmed using the EDX spectrum (Fig. 3g). The atomic percentage was about 70.35 and 24.21% of O and C in the EDS spectrum, while the Ce concentrations were *ca.* 0.36, 0.64 and 1.06 wt%, respectively. The elemental mapping obtained showed that Zr, Ce, O and C were uniformly dispersed in the Ce–ZrO₂–GO nanocomposite (Fig. 3h).

3.5 Bandgap Determination

The bandgap energy (E_g), which is the difference between the valence band (VB) and CB was used to characterise the band structure of Ce–ZrO₂–GO nanocomposites [51]. The bandgap energy of the as-fabricated materials was obtained from the Kubelka–Munk formula [52]:

$$(\alpha h\nu)^{1/n} = A(h\nu - E_g) \quad (1)$$

where h is Planck's constant, ν is the photon's frequency, α is the absorption coefficient, E_g is the band gap and A is the slope of the Tauc plot in the linear region. The value of the exponent denotes the nature of the electronic transition, whether allowed or forbidden and whether direct or indirect [53]. $n = 1/2$ and 2 for direct and indirect transitions, respectively [53]. The optical transition for pure ZrO₂ was indirectly allowed since the n value was 2. Therefore,

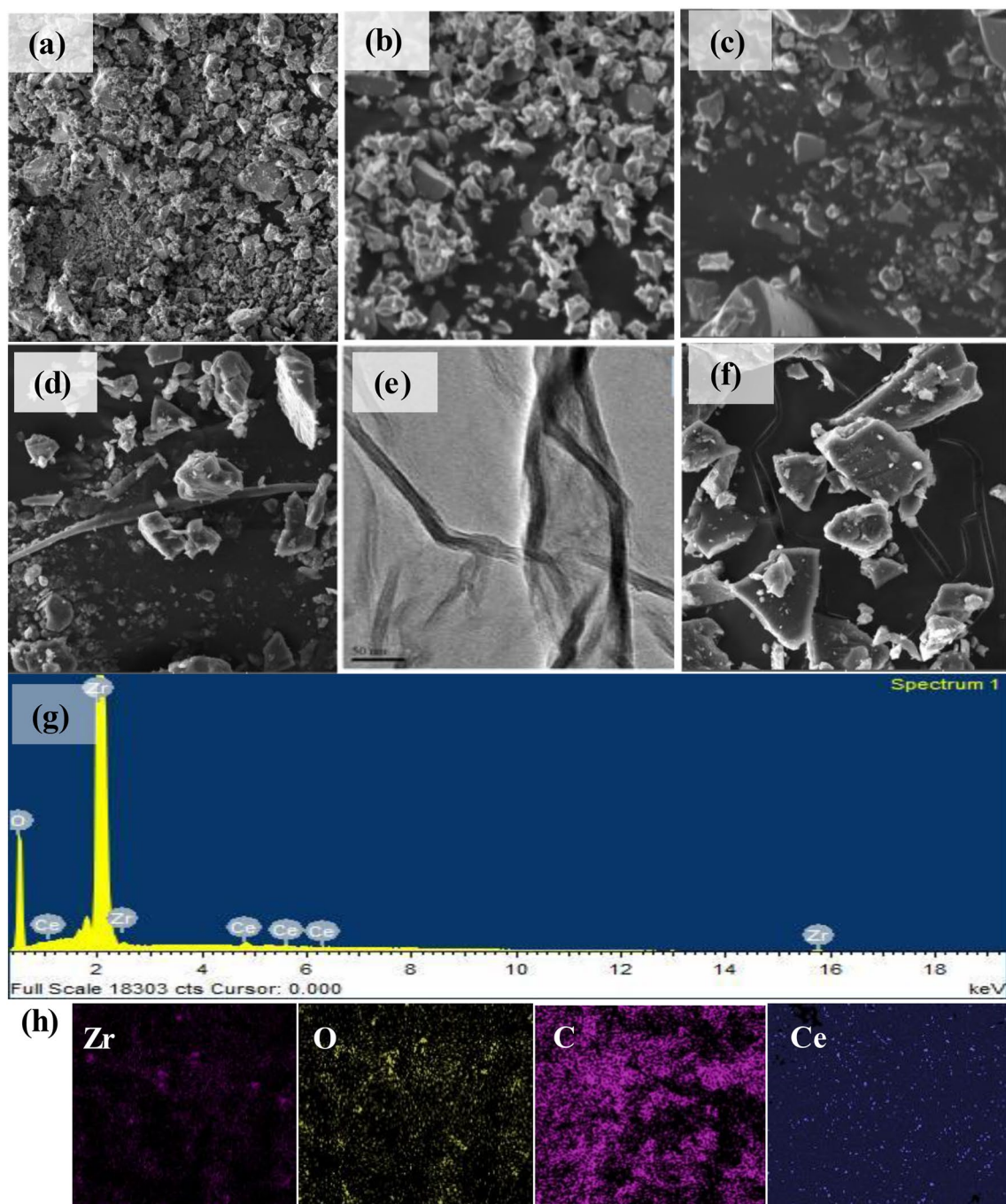


Fig. 3 SEM images of **a** ZrO₂, **b** ZrO₂-GO and **c** Ce-ZrO₂-GO; TEM images of **d** ZrO₂, **e** GO and **f** Ce-ZrO₂-GO; **g** EDX spectrum of Ce-ZrO₂-GO and **h** Elemental mapping of Ce-ZrO₂-GO

the bandgap energies were evaluated from a plot of $(ah\nu)^{1/2}$ versus photon energy, and the intercept of the tangent to the x-axis gave a better estimation of the bandgap energy for pure ZrO₂, GO sheets, ZrO₂-GO and Ce-ZrO₂-GO nanocomposite [17]. The bandgap energies of pure ZrO₂

and ZrO₂-GO nanocomposite were calculated as 5.68 and 3.29 eV, respectively (Fig. 4).

The reduced E_g is because of the chemical bonding between the active sites of GO and ZrO₂ [54]. The bandgap energy of ZrO₂-GO nanocomposite was very close to the 3.25 eV previously reported [55]. As obtained from the Tauc plot, the E_g values of Ce-ZrO₂-GO (0.3% Ce), Ce-ZrO₂-GO

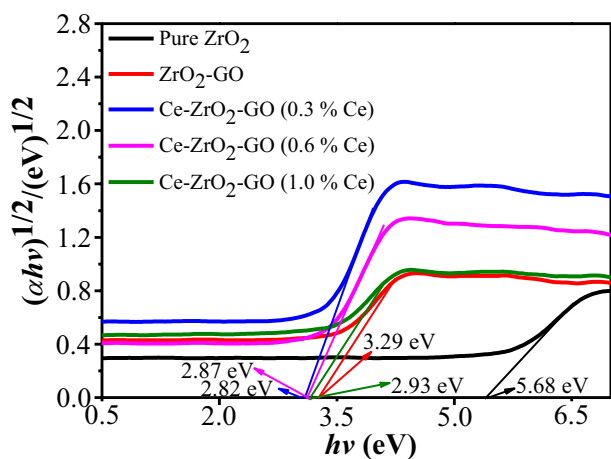


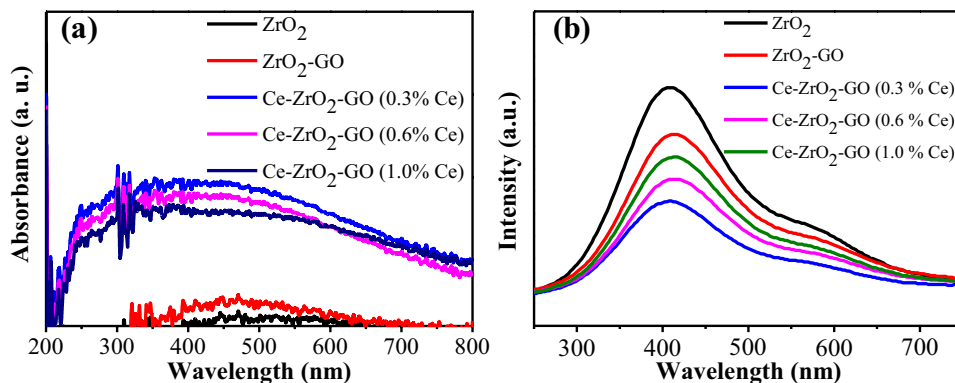
Fig. 4 Plot of $(\alpha hv)^{1/2}$ against hv for pure ZrO_2 , ZrO_2 -GO and Ce- ZrO_2 -GO (with variable concentrations of Ce)

(0.6% Ce) and Ce- ZrO_2 -GO (1.0% Ce) nanocomposites were 2.82, 2.87 and 2.93 eV, respectively (Fig. 4). The narrow E_g of Ce- ZrO_2 -GO nanocomposite might be ascribed to the defective energy levels and electronic interaction [56]. Based on the above results, the favourable E_g values of Ce- ZrO_2 -GO nanocomposite compared with the pure ZrO_2 and ZrO_2 -GO nanocomposite clearly revealed that the Ce- ZrO_2 -GO nanocomposites could have a better electron migration property, and therefore, could act as an efficient photocatalyst material with improved photoactivity under simulated light irradiation [51].

3.6 Optical Analysis

The performance of visible light absorption is a significant contributor to accessing the optical property of semiconductor-based photocatalyst materials [57]. The optical performance of the as-synthesised nanocomposites was measured with the UV-Vis absorbance spectroscopy. The absorbance spectra of ZrO_2 and Ce- ZrO_2 -GO nanocomposite with variable concentrations of Ce are given in Fig. 5a.

Fig. 5 **a** UV-Vis absorbance spectra and **b** photoluminescence (PL) spectra of ZrO_2 , ZrO_2 -GO and Ce- ZrO_2 -GO (with variable concentrations of Ce)



Both pure ZrO_2 and ZrO_2 -GO nanocomposite showed weak absorption, which was attributed to their wide bandgap energy (Fig. 5a). The Ce- ZrO_2 -GO nanocomposites showing a broader optical-response range compared with pure ZrO_2 and ZrO_2 -GO was due to the $\pi \rightarrow \pi^*$ transitions of the C=C bond [21]. The improved photoactivity was because of the highly visible light absorption edge and reduce electron-hole pairs recombination rate of ZrO_2 by the introduced Ce and GO sheets. The incorporation of different concentrations of Ce significantly influenced the optical performance of visible light absorption of Ce- ZrO_2 -GO nanocomposites (Fig. 5a). The Ce- ZrO_2 -GO (0.3% Ce) nanocomposite showed the highest visible light absorption and this suggested that the optimum Ce concentration for optimum visible light absorption was 0.3%. Thus, the obtained Ce- ZrO_2 -GO (0.3% Ce) nanocomposite was expected to show an improved photoactivity than bulk ZrO_2 under simulated visible light irradiation.

3.7 The Photoluminescence (PL) Analysis

In the photocatalysis process, the photogenerated charge carrier recombination is among the key issue responsible for the low photocatalysis efficiency. Generally, PL analysis can offer in-depth insights into the separation and the recombination rate of photoexcited charge carriers in the photocatalysts [58]. Stronger PL intensity usually indicates a faster charge carrier recombination rate. Figure 5b shows the PL spectra of the fabricated photocatalyst. Due to $\pi-\pi^*$ electronic transitions, a strong peak at 416 nm was detected in all the as-prepared photocatalysts. The PL spectra of pure ZrO_2 showed a weak emission peak in the visible spectrum, which was because of the fast recombination of charge carriers. The PL intensity of ZrO_2 was reduced after the introduction of GO sheets, whereas with the addition of Ce, a further strong reduction in PL was observed. This significant PL quenching was attributed to the efficient electron migration from ZrO_2 onto GO sheets via Ce ion. Thus, the PL spectrum of ZrO_2 -GO nanocomposite was significantly quenched compared to pure ZrO_2 , which was because of

the interactions between the GO sheets and the excited state of ZrO_2 , and the interfacial charge migration in ZrO_2 -GO nanocomposite. Moreover, the hybrid Ce- ZrO_2 -GO nanocomposite showed more quenching of PL emission compared to ZrO_2 -GO, which revealed that Ce- ZrO_2 -GO had a better electrical conductivity than ZrO_2 , thus leading to better separation of charge carriers. Therefore, the interaction among GO sheets, ZrO_2 and Ce ion in the hybrid Ce- ZrO_2 -GO nanocomposite could contribute to the efficient separation, thereby prolonging the lifetime of charge carriers, and further improved the photodegradation efficiency. The highest PL quenching occurred in Ce- ZrO_2 -GO (0.3% Ce) nanocomposite, suggested that the 0.3% Ce was the optimal concentration to obtain the best efficiency of charge carrier migration. Herein, when the concentration of Ce ion was excessive, the number of active sites capturing the photoexcited electron was reduced by increasing the size of Ce nanoparticles. Thus, excessive Ce ions could cover the ZrO_2 surface, leading to an increased recombination rate of charge carriers and reduced photoactivity of the photocatalysts [59].

3.8 Assessment of Photocatalytic Performance

The photoactivity of the as-fabricated pure ZrO_2 , ZrO_2 -GO and Ce- ZrO_2 -GO (with variable concentrations of Ce)

were tested by the photodegradation of EY dye under UV light irradiation. In addition, dark absorption of EY dye was accessed for 60 min to evaluate self-degradation. The absorbance remained virtually the same for bulk ZrO_2 , ZrO_2 -GO and Ce- ZrO_2 -GO (with variable concentrations of Ce) photocatalysts, suggests that there is no absorption in the dark. The photocatalytic degradation efficiency of the as-fabricated photocatalyst was evaluated following Eq. (2) [60]:

$$\text{Photodegradation}(\%) = (1 - C/C_0) \times 100\% \quad (2)$$

where C and C_0 represent the residual concentration of EY dye at different light intervals and the concentration of EY dye at adsorption equilibrium, respectively [60]. Pure ZrO_2 nanoparticles showed the lowest photodegradation performance (Fig. 6a).

For pure ZrO_2 nanoparticles, the degradation rate was only 16% (see Table 1) after 210 min of simulated light irradiation.

The introduction of GO sheets significantly accelerated the photodegradation process of ZrO_2 -GO nanocomposite. The percentage photodegradation was increased to 31% of EY dye when GO was added, signifying the substantial effect of GO in increasing the photodegradation of ZrO_2 -GO nanocomposite. The promoted photoactivity of ZrO_2 -GO nanocomposite was ascribed to the close contact between the

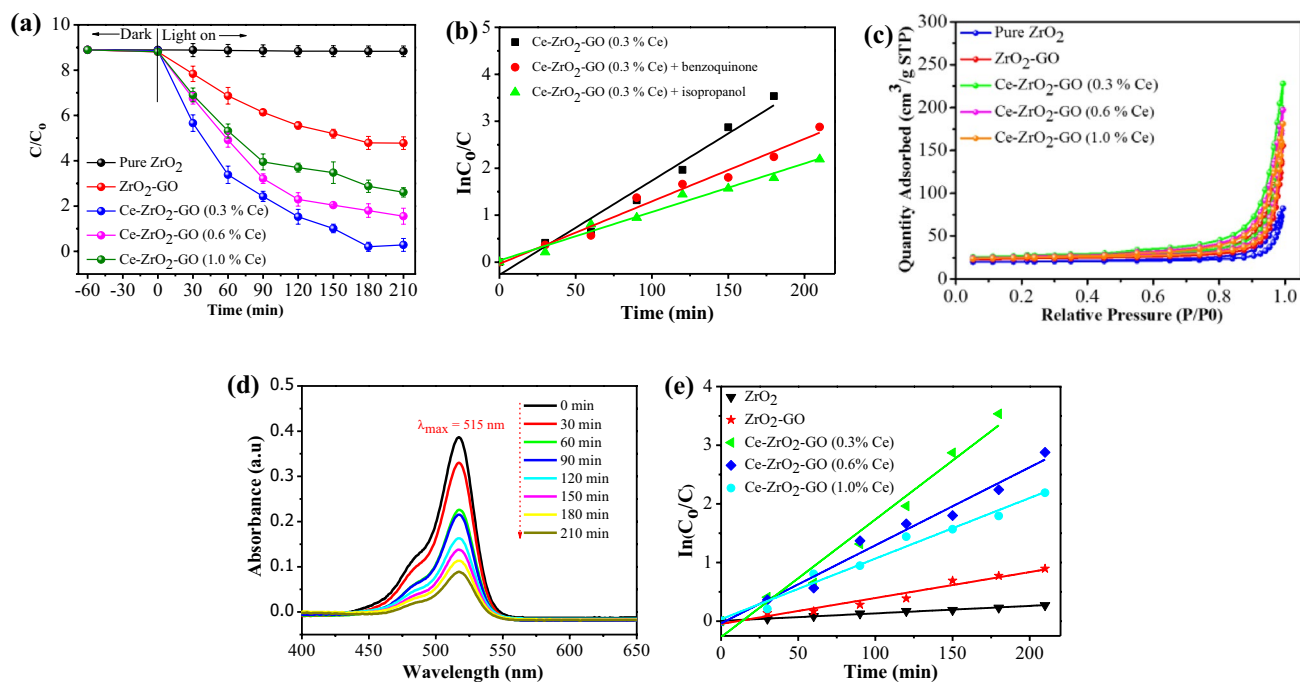


Fig. 6 **a** Photocatalytic degradation of eosin yellow dye under UV light irradiation of pure ZrO_2 , ZrO_2 -GO and Ce- ZrO_2 -GO (with variable concentrations of Ce), **b** plot of $\ln(C_0/C)$ vs. light irradiation time for photodegradation of eosin yellow solution containing pure ZrO_2 , ZrO_2 -GO and Ce- ZrO_2 -GO (with variable concentrations of

Ce), **c** nitrogen adsorption-desorption of the fabricated photocatalysts, **d** visible light irradiation of eosin yellow solution in the presence of Ce- ZrO_2 -GO (0.3% Ce) photocatalyst and **e** role of active species on the photodegradation of eosin yellow solution

Table 1 Some parameters for pure ZrO₂, ZrO₂–GO and Ce–ZrO₂–GO (with variable concentrations of Ce)

Sample	S_{BET} (m ² g ⁻¹)	Pore volume	Pore size	Degradation (%)	k (min ⁻¹)	R^2
ZrO ₂	26.79	0.25	4.19	16	8.95×10^{-4}	0.9975
ZrO ₂ –GO	56.73	0.29	3.89	31	3.11×10^{-3}	0.9828
Ce–ZrO ₂ –GO (0.3% Ce)	86.45	0.32	4.51	100	1.43×10^{-2}	0.9922
Ce–ZrO ₂ –GO (0.6% Ce)	73.96	0.41	3.65	87	9.40×10^{-3}	0.9806
Ce–ZrO ₂ –GO (1.0% Ce)	67.32	0.39	3.48	85	7.30×10^{-3}	0.9933

ZrO₂ and GO sheets. In contrast, Ce–ZrO₂–GO nanocomposites with several concentrations of Ce showed improved photoactivity for EY dye degradation than pure ZrO₂ and ZrO₂–GO. When the concentration of Ce was less than 0.3%, the photodegradation was enhanced. Nonetheless, due to the accessibility of active sites and efficient penetration of light on the ZrO₂ surface, any further increase in the amount of Ce during the co-precipitation fabrication reduced the photodegradation performance. This is comparable with other studies [61]. Interestingly, the Ce–ZrO₂–GO nanocomposites with 0.3% of Ce showed the highest photoactivity with almost 100% photodegradation of EY dye in 210 min. This high efficiency for EY degradation by Ce–ZrO₂–GO nanocomposites was found to be slightly higher compared with that of GO–Fe₃O₄@ZrO₂ (98%) [21], but comparable to the GO–Ag₃PO₄ nanocomposite with 0.26 wt% GO [50]. This clearly showed that the Ce–ZrO₂–GO (0.3% Ce) nanocomposite rendered the best catalytic efficiency. The photodegradation efficiency of the catalyst was due to the ratio of Ce and Zr in the nanocomposite. As expected, the Ce seems to act as a charge carriers scavenger to minimise their recombination rate [31].

3.9 Kinetics Studies

The kinetics of EY dye degradation under light irradiation was also investigated. As revealed in Fig. 6b, the kinetics of EY dye degradation was pseudo first-order reaction, since pure ZrO₂, ZrO₂–GO and Ce–ZrO₂–GO (with variable concentrations of Ce) showed linear lines [60]. The first-order kinetics indicated that the photocatalytic reaction rate was mainly reliant on the absorption efficiency and light intensity of the EY dye.

The photodegradation rate constant, k is evaluated from the kinetic method:

$$\ln(C/C_0) = -kt \quad (3)$$

where C and C_0 are the concentration of a reaction time t and initial concentration, respectively [60]. The rate constants are estimated as 8.95×10^{-4} and 3.11×10^{-3} min⁻¹ for pure ZrO₂ and ZrO₂–GO nanocomposite, respectively. The photoactivity of ZrO₂–GO nanocomposite is about 3.47-fold compared with pure ZrO₂ nanoparticles. The rate constants

for Ce–ZrO₂–GO (0.3% Ce), Ce–ZrO₂–GO (0.6% Ce) and Ce–ZrO₂–GO (1.0% Ce) nanocomposites were calculated as 1.43×10^{-2} , 9.40×10^{-3} and 7.30×10^{-3} min⁻¹, respectively. The apparent rate constants of Ce–ZrO₂–GO (0.3% Ce) is 15.98, 1.52 and 1.96 times higher compared with ZrO₂ nanoparticles, Ce–ZrO₂–GO (0.6% Ce) and Ce–ZrO₂–GO (1.0% Ce) nanocomposites, respectively. Generally, a higher BET surface area (S_{BET}) could promote the photoactivity of the photocatalyst [62], since the photocatalytic process is linked with the adsorption and desorption of pollutants on the photocatalyst surface [63]. To evaluate the effect of GO sheets and Ce dopant on the BET surface area of ZrO₂, nitrogen adsorption–desorption isotherm is employed (Fig. 6c).

The Ce–ZrO₂–GO (0.3% Ce) nanocomposite has S_{BET} of 86.45 m² g⁻¹ (Table 1) and this is about 3.23-fold higher compared with pure ZrO₂ (26.79 m² g⁻¹). The higher surface area was ascribed to the coupled GO sheets, which had a large exposed area, leading to improved adsorption of pollutants and most active sites on the nanocomposite surface [64]. The high k -value of Ce–ZrO₂–GO (0.3% Ce) nanocomposite is ascribed to the combined synergy of both the optimum Ce concentration and GO in the nanocomposite. In conclusion, the incorporation of optimum amounts of Ce and GO on the ZrO₂ nanoparticle resulted in an enhancement of photocatalytic pollutant degradation performance.

3.10 EY Photodegradation Profile

Figure 6d shows the absorption spectra of EY dye solution of the as-prepared Ce–ZrO₂–GO and exposure to the irradiation of light under different durations. The absorption peak of 515 nm corresponding to the EY dye was used to check the photodegradation process. This absorption peak was comparable with other studies [63]. The EY photodegradation profile (Fig. 6d) showed a constant decrease in the highest absorption wavelength ($\lambda = 515$ nm) of EY over a period of exposure time (0–180 min), indicating the direct relationship between the dye degrading and exposure time. This occurrence was ascribed to the presence of Ce, which scavenge the photoexcited electrons and reduce their recombination with the holes, thereby promoting the photoactivity of the photocatalyst.

3.11 Experiment for Radical Scavenging

The radical trapping experiment was carried out to comprehend the role of key active species involved in the photodegradation of EY dye over ZrO_2 photocatalyst. This was done using benzoquinone (BQ) [65] and isopropanol (IPA) as $\text{O}_2^{\cdot-}$ and HO^\bullet scavengers, respectively [66]. As given in Fig. 6e, the photoactivity of Ce– ZrO_2 –GO (0.3% Ce) nanocomposite is clearly suppressed by adding BQ or IPA. The degradation rate constant of EY dye decrease of $8.73 \times 10^{-3} \text{ min}^{-1}$ (42% degradation) in the existence of BQ (Table 2) compared with the $1.43 \times 10^{-2} \text{ min}^{-1}$ (58% degradation) when BQ was absent.

The maximum degradation in the presence of BQ is lower than the 58.2% reduction in photodegradation efficiency with the addition of BQ to Bi– TiO_2 – ZrO_2 nanocomposite [45]. Likewise, adding an IPA decreased the photocatalytic degradation rate to $7.26 \times 10^{-3} \text{ min}^{-1}$, which was ~ 1.96 times slower compared to the photodegradation without IPA. The obtained result signifies that both HO^\bullet and $\text{O}_2^{\cdot-}$ radicals are responsible for the degradation of EY dye. This is similar to other studies [67].

3.12 Total Organic Carbon analysis (TOC) Analysis

General, photodegradation does not indicate complete mineralization since the pollutants could be photocatalytically degraded into small molecules. Fusion UV/persulfate TOC analysis was performed to study the extent of mineralisation of eosin yellow dye by the photocatalyst [68]. The experiment was performed over a period of 5 h. According to Fig. 7a, 76% TOC removal was reached after 5 h showing

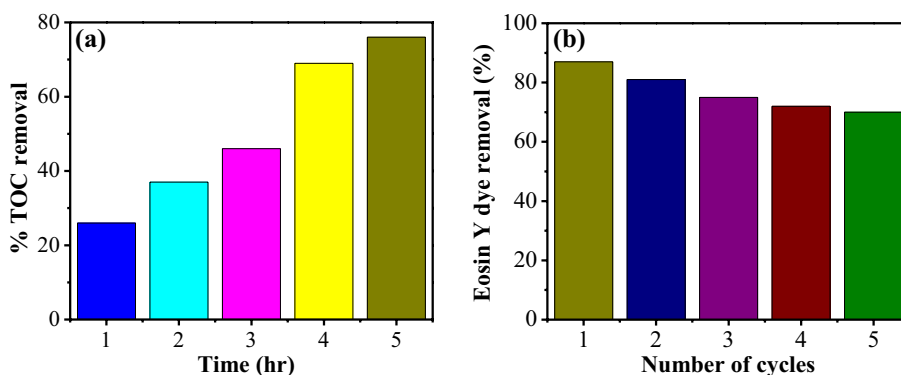
that a considerable degree of mineralisation of the dye by the nanocomposite was achieved within 5 h.

This indicated that the reactive species produced by Ce– ZrO_2 –GO (0.3% Ce) nanocomposite could not only photodegrade EY dye, but also can efficiently decompose EY dye into CO_2 and water [69]. Although the Ce– ZrO_2 –GO (0.3% Ce) nanocomposite exhibited an enhanced photoactivity, higher stability is vital in view of its industrial applications. Therefore, to promote the reusability efficiency from the industrial perspective, the photocatalyst was anticipated to be photostable throughout the reaction. Under the same condition, the recyclability experiment was performed in a five-run cycling test to study the performance of the Ce– ZrO_2 –GO (0.3% Ce) nanocomposite. The as-prepared nanocomposite was recycled, cleaned and dried for each batch of the experiment. The photodegradation of EY dye in the first cycle was 87%, which was then reduced in the next cycles and finally reached 70% after the fifth cycle (Fig. 7b). The reduction in the photocatalytic efficiency after its recycled was induced by the reduction of the number of active sites accessible on the Ce– ZrO_2 –GO (0.3% Ce) nanocomposite surface after each cycle of photodegradation. However, there was no much loss of performance after five cycles of photodegradation reaction, which signifies the stable structure of Ce– ZrO_2 –GO (0.3% Ce) nanocomposite during the degradation process. This indicated that the Ce– ZrO_2 –GO (0.3% Ce) nanocomposite maintained a good performance towards the degradation of EY dye even after the fifth cycle.

Table 2 The rate of photocatalytic degradation in the presence or absence of radical scavenger

Nanocomposite	Photodegradation (%)		k (min^{-1})	R^2
	Scavengers	No scavengers		
Ce– ZrO_2 –GO (0.3% Ce)		100	1.43×10^{-2}	0.9922
Ce– ZrO_2 –GO (0.6% Ce)+BQ	42	58	8.73×10^{-3}	0.9907
Ce– ZrO_2 –GO (1.0% Ce)+IPA	51	49	7.26×10^{-3}	0.9843

Fig. 7 a Percentage Total Organic Carbon removal and b recycle test of Ce– ZrO_2 –GO (0.3% Ce) nanocomposite for eosin yellow degradation under simulated light irradiation



3.13 Theoretical Study

3.13.1 Catalytic Stability

The Ce–ZrO₂–GO nanocomposite was constructed with a 4×2 supercells of ZrO₂ and 4×4 supercells of GO sheets. This gave rise to a 3.13% lattice mismatch, which established the fabrication of the ZrO₂–GO and Ce–ZrO₂–GO photocatalyst [70]. The interactions between the ZrO₂ (or Ce–ZrO₂) and GO sheets determines the photocatalytic efficiency and the origin of charge transfer of the as-prepared nanocomposite. Therefore, the interface adhesion energy and interlayer spacing were accessed to examine the physical properties of the as-fabricated nanocomposite using a hybrid DFT study. In this study, the interlayer spacing was determined as the distance between the bottom-most and top-most atoms of pure ZrO₂ (or Ce–ZrO₂) and GO sheets, respectively. For the ZrO₂–GO and Ce–ZrO₂–GO nanocomposites, the interlayer spacing was calculated as 3.19 and 3.06 Å, respectively. This agreed with other GO-based photocatalysts [71, 72]. Since the separation characterises the strength of interfacial interactions, the Ce–ZrO₂–GO nanocomposite with a smaller interlayer spacing suggest a stronger interfacial interaction than the ZrO₂–GO nanocomposite [73].

Since the ZrO₂–GO and Ce–ZrO₂–GO nanocomposites were successfully fabricated, the catalytic stability and possibility of the as-prepared nanocomposites were evaluated by comparing the interface adhesion energy:

$$E_{ad} = [E_{ZrO_2-GO} - E_{ZrO_2} - E_{GO}]/S \quad (4)$$

$$E_{ad} = [E_{Ce-ZrO_2-GO} - E_{ZrO_2} - E_{GO} - \mu_{Ce} + \mu_{Zr}]/S \quad (5)$$

where E_{ZrO_2-GO} , E_{ZrO_2} , E_{GO} and E_{Ce-ZrO_2-GO} represent the formation energies of ZrO₂–GO, ZrO₂, GO sheets and Ce–ZrO₂–GO nanocomposite, respectively. μ_{Ce} and μ_{Zr} are the chemical potential of the Ce dopant and host Zr ion, respectively. S is the surface area of the plane.

3.13.2 Electronic Band Structures and Projected Density of States (PDOS)

To examine the effect of GO hybridisation on the electronic structures of ZrO₂, the electronic band structure and PDOS of ZrO₂ and GO before and after the formation of the as-fabricated photocatalysts (Fig. 8).

For pure ZrO₂, the bandgap energy of 5.01 eV was indirect with the valence band maximum (VBM) positioned at Γ point and primarily contributed by the O–2p state, while the conduction band minimum (CBM) was located on the B point and mainly dominated by Zr–4d state (Fig. 8a). The band structure of GO showed that the CBM and VBM was located at Y and Γ points, respectively, which confirmed an indirect bandgap semiconductor and the bandgap energy was calculated as 2.75 eV (Fig. 8b). In addition, as revealed in Fig. 8b, the CBM consisted of C–2p and C–2s states, whereas the VBM mostly dominated by O–2p and O–2s states. The theoretical calculations confirmed the indirect bandgap character of ZrO₂–GO nanocomposite where the VBM resides on the Γ point, while the CBM positioned at

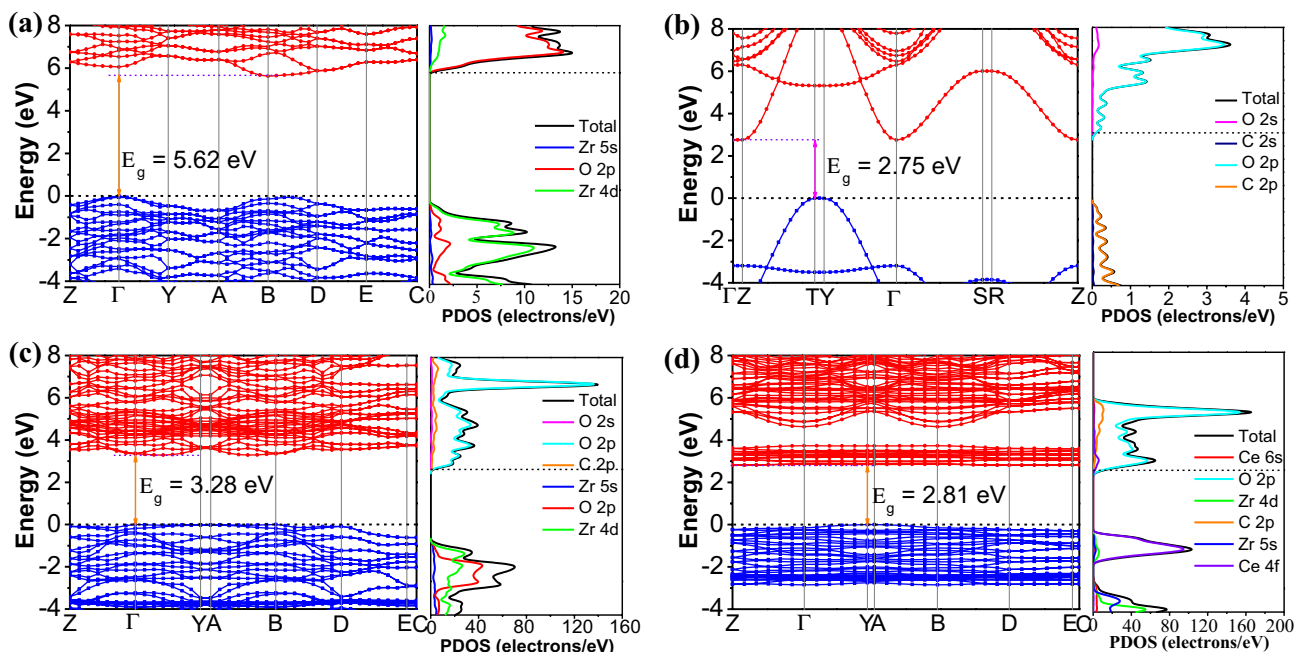


Fig. 8 The PDOS and band structure of **a** bulk ZrO₂, **b** graphene oxide, **c** ZrO₂–GO and **d** Ce–ZrO₂–GO photocatalysts

some point between Γ and Y points. The bandgap energy was calculated as 3.28 eV. For ZrO_2 -GO, the CBM consisted of O-2p state mixed with C-2p state of GO sheets, while the VBM was contributed by O-2p state of ZrO_2 , see Fig. 8c. In the band structure of Ce- ZrO_2 -GO nanocomposite, the CBM was situated along the Z - D line, while the VBM was located along the Y - A line in the Brillouin Zone. This reveals an indirect bandgap semiconductor with an E_g of 2.81 eV. Figure 8d showed that Ce-4f state significantly hybridised with the C-2p and O-2p state of GO sheets at the CBM. Moreover, the VBM was contributed by the O-2p state of ZrO_2 with hybridisation of Ce-4f and Zr-4d states. The calculated E_g values of pure ZrO_2 , ZrO_2 -GO and Ce- ZrO_2 -GO nanocomposites were consistent with the experimental values and this confirmed the accuracy and reliability of the theoretical method and parameters employed in this study.

3.13.3 Charge Density Distribution

The orbital contributions of the CBM and VBM can be further understood from the charge density distribution of the highest occupied level (HOL) and the lowest unoccupied level (LUL), see Fig. 9.

The charge density distribution suggested that the orbital density of the HOL and LUL for ZrO_2 and GO sheets highlighted the occurrence of electron or hole donor-acceptor states in the nanocomposites. In the ZrO_2 -GO, the lowest unoccupied level was localised around the GO sheets with the involvement of O-2p and C-2p states, whereas the Zr-4d and O-2p states of ZrO_2 constituted the major hole density distribution of the HOL (Fig. 9a, c). The charge density distribution of Ce- ZrO_2 -GO nanocomposite predicted the contribution of Ce ions (Ce-4f state) as part of the HOL and LUL orbitals, which was different from that of ZrO_2 -GO. Both nanocomposites predicted that Zr-4d and O-2p states constitute the HOL and LUL, respectively, which represent hole and electron acceptor states (Fig. 9b, d). This suggested

that when Ce- ZrO_2 -GO nanocomposite was irradiated with solar light, the Zr-4d and O-2p electrons in the HOL were photoexcited into the O-2p and C-2p states in the LUL via the Ce-4f state. Thus, ZrO_2 could serve as a visible-light sensitizer in the nanocomposite to enhance not only the separation of charge carriers, but also the visible light photoactivity. The electron density obviously predicted the key constituents of energy levels and was in agreement with the DOS results.

3.13.4 Charge Transfer and Mechanism Analysis

The calculated Fermi energies of pure ZrO_2 , GO sheets, and the ZrO_2 -GO and Ce- ZrO_2 -GO nanocomposites were -4.17 , -2.24 , -1.95 and -1.49 eV, respectively. Such a shift in the Fermi energy level revealed a charge density redistribution of charges after ZrO_2 or Ce- ZrO_2 was adsorbed onto the GO sheets and this was confirmed by plotting the three-dimensional (3D) charge, see Fig. 10.

This was evaluated by subtracting the charge density of the nanocomposites from that of the individual monolayers making up the nanocomposites. The green and purple regions represent charge density depletion and accumulation, respectively. As given in Fig. 10, the charge redistribution density led to the polarisation of electrons, and the formation of an interface dipole. Moreover, the charge redistribution at the surface suggested an interfacial charge migration owing to the coupling of GO and ZrO_2 or Ce- ZrO_2 . Figure 10a revealed that the charge density largely accumulated in the interface region of ZrO_2 -GO and reduced a bit in ZrO_2 phase, while there was virtually no or little charge migration of the O atoms in the graphene oxide far away from the interface. However, in the Ce- ZrO_2 -GO nanocomposites, charge redistribution was observed on the O atoms in the GO sheets far away from the interface, since the Ce dopant improved the intermolecular interaction (Fig. 10b). In both nanocomposites, a

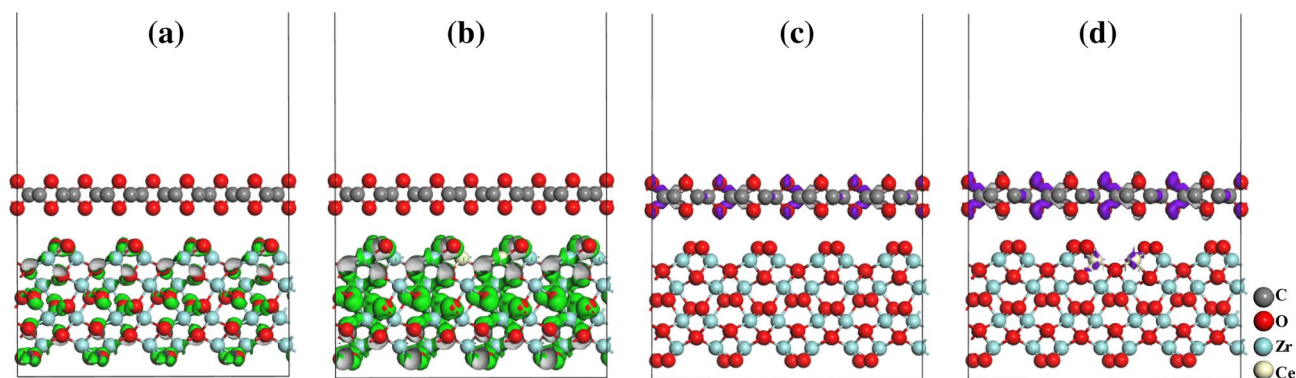


Fig. 9 The electrons and holes density distribution of highest occupied level (a, b) and lowest unoccupied level (c, d) with an isovalue of 0.07 e^{-3} for ZrO_2 -GO and Ce- ZrO_2 -GO nanocomposites

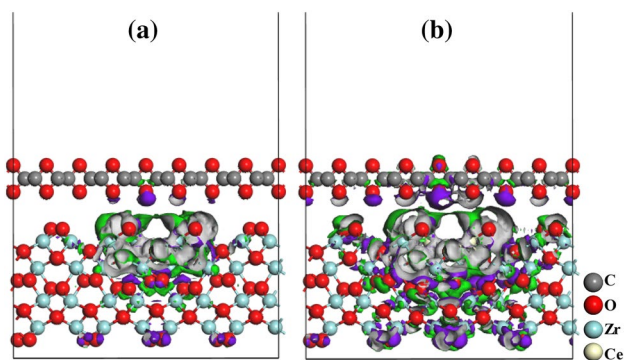


Fig. 10 The 3D charge density differences of **a** ZrO₂-GO and **b** ZrO₂-GO-GO. The isosurface value was set at 0.006 e Å⁻³

strong charge accumulation was observed above the oxygen atoms close to the interface region of GO sheets and Zr atoms at the bottom of ZrO₂, while the charge depletion appeared on the surface facing the ZrO₂ [74]. The charge density redistribution obviously revealed that the charge density redistribution increase on the ZrO₂, while the redistribution at GO was less intense when Ce ion was present. Thus, the interface attracted both electrons and holes, which is vital for the separation of charge carriers

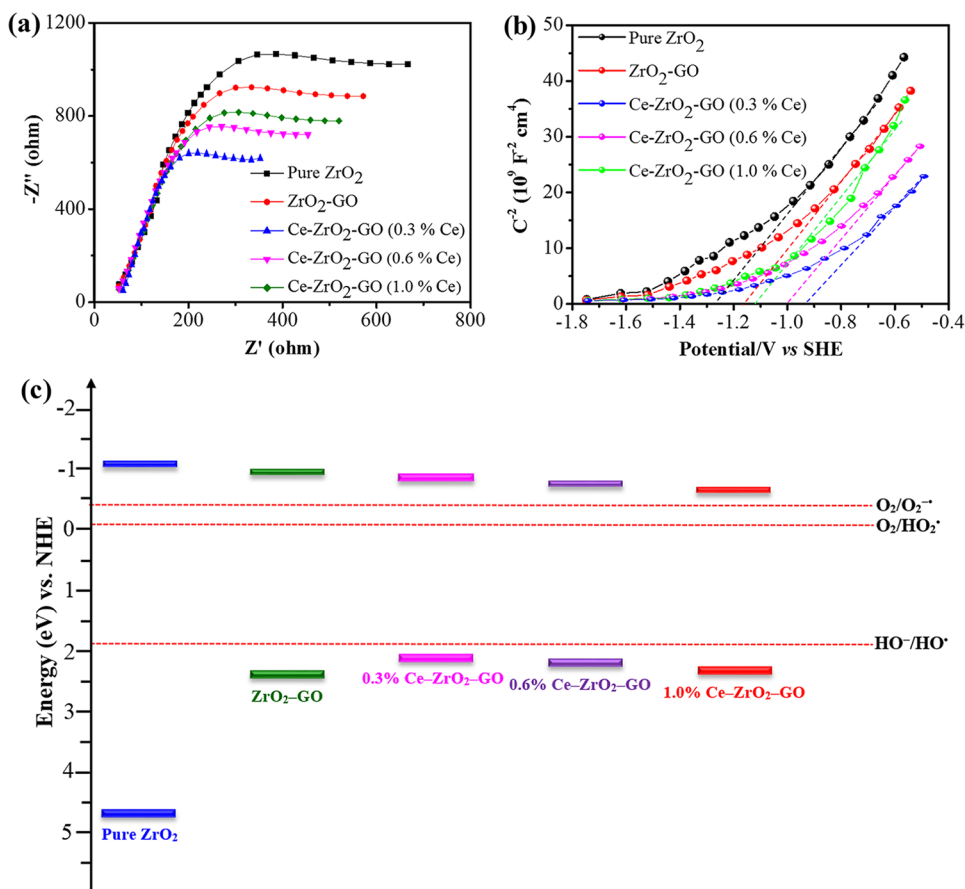
at the interface. The Mulliken charge analysis revealed a 0.35 electrons migration at the Ce–ZrO₂–GO interface, while only 0.09 electrons were transferred from GO sheets to ZrO₂. This was due to the strong interfacial adhesion of Ce–ZrO₂–GO nanocomposite.

3.14 Electrochemical Impedance Spectroscopy Analysis

The separation efficiency of charge carriers at the interface is a vital factor in photocatalysis. To determine the migration and separation of charge carriers between the photocatalysts, electrochemical impedance spectroscopy was used [75]. In this study, an EIS Nyquist plot was used to examine the charge separation and migration processes at the interface region of electrode–electrolyte [76]. Generally, a smaller arc radius signifies higher migration of charge carriers [77]. Figure 11a shows the Nyquist plot of bulk ZrO₂, ZrO₂-GO and Ce–ZrO₂-GO nanocomposites with variable concentrations of Ce.

As shown in Fig. 11a, incorporation of GO into ZrO₂ dramatically enhanced the separation and migration efficiency of charge carriers *via* an interfacial interaction between GO and ZrO₂. Moreover, the arc radius of Ce–ZrO₂-GO

Fig. 11 **a** Electrochemical impedance spectroscopy, **b** Mott–Schottky plot and **c** the band alignment of the prepared photocatalysts



photocatalyst with variable concentrations of Ce was smaller than pure ZrO_2 and ZrO_2 -GO nanocomposite, signifying the lower resistance value for charge migration, as well as effective separation and fast interfacial transfer of charge carriers. The Ce- ZrO_2 -GO (0.3% Ce) nanocomposite showed the lowest semicircle diameter among all the Ce- ZrO_2 -GO nanocomposites, which resulted enhanced the efficiency of charge carrier migration and photoactivity [78]. This agreed with the above EY photodegradation and PL results. From the above EIS study, the amount of the Ce ions influence the photoactivity and charge migration kinetics of Ce- ZrO_2 -GO nanocomposites.

3.15 Mott-Schottky Plot Analysis

The effects of Ce doping and GO sheets with the flat-band potential (E_{fb}) of ZrO_2 was evaluated using Mott-Schottky equation [79]:

$$\frac{1}{C^2} = \frac{2}{e\epsilon\epsilon_0N_D} \left(E - E_{fb} - \frac{k_B T}{e} \right) \quad (14)$$

where C , ϵ , ϵ_0 , N_D , E , E_{fb} , k_B , T and e are the space charge capacitance, dielectric constant, permittivity of free space, electron carrier density, external applied potential, flat band potential, Boltzmann constant, temperature and elemental charge of the photocatalyst, respectively. The E_{fb} values were obtained by taking the x -intercept of a linear fit to Mott-Schottky plot against the applied potential, as shown in Fig. 11b. The E_{fb} of pure ZrO_2 , ZrO_2 -GO, Ce- ZrO_2 -GO (0.3% Ce), Ce- ZrO_2 -GO (0.6% Ce) and Ce- ZrO_2 -GO (1.0% Ce) were *ca.* -1.27 , -1.15 , -1.11 , -1.01 and -0.92 V *vs.* SCE, and are *ca.* -1.03 , -0.91 , -0.87 , -0.77 and -0.68 V versus normal hydrogen electrode (NHE), respectively, where $\text{NHE} = \text{SCE} + 0.24$ V. With the assumption that the E_{fb} lied at the same potential with that of CB edge [80], the VB level was obtained by subtracting the E_g energy from the CB level. The VB positions of pure ZrO_2 , ZrO_2 -GO, Ce- ZrO_2 -GO (0.3% Ce), Ce- ZrO_2 -GO (0.6% Ce) and Ce- ZrO_2 -GO (1.0% Ce) were calculated as 4.65, 2.38, 2.06, 2.10 and 2.14 eV *vs.* NHE, respectively. The band alignment of the as-fabricated photocatalysts were schematically shown in Fig. 11c. Moreover, the photoinduced electrons in the CB of as-fabricated nanocomposites could reduce the dissolved O_2 to produce active $\text{O}_2^{\cdot-}$ anion radical owing to the more negative potential of E_{CB} of the as-fabricated nanocomposites compared to the $\text{O}_2/\text{O}_2^{\cdot-}$ potential (-0.33 eV). Moreover, the holes in the VB of the as-fabricated nanocomposites could effectively oxidise the HO^- ion to generate HO^{\cdot} radical, since E_{CB} was more positive compared to the potential of $\text{HO}^-/\text{HO}^{\cdot}$ ($+1.99$ eV). Clearly, the results suggest that the h^+ , HO^{\cdot} and $\text{O}_2^{\cdot-}$ radicals could be the reactive species requires for the photodegradation of EY dye.

3.16 Photocatalytic Mechanism

The VB and CB edge potential of ZrO_2 were evaluated by the Mulliken electronegativity theory, as given in Eqs. (11) and (12) [81]:

$$E_{VB} = \chi - E^o + 0.5E_g \quad (11)$$

$$E_{CB} = E_{VB} - E_g \quad (12)$$

where E_{VB} , E_{CB} , χ , E^o and E_g represent the VB edge, CB edge, electronegativity of the studied semiconductors, energy of free electrons on the hydrogen scale (*ca.* 4.5 eV) and the calculated bandgap from Kubelka-Munk, respectively. The electronegativity value of ZrO_2 is 5.91 [82]. The CB and VB potentials of ZrO_2 were -1.12 and 3.94 eV, respectively.

In this study, the mechanistic pathways were presented in the form of direct semiconductor photoexcitation of EY dye. The direct semiconductor photoexcitation photocatalytic mechanism of Ce- ZrO_2 -GO nanocomposite was proposed based on the interfacial charge migration and change in the Fermi energy level, as given in Fig. 12.

As shown in Fig. 12, when the Ce- ZrO_2 -GO nanocomposite was exposed to visible light, the photogenerated electrons on the CB of ZrO_2 tend to migrate to GO sheets via metallic Ce ion, since the CB potential of ZrO_2 was higher than that of GO sheets [83]. Here, GO sheets exhibited an excellent electron storage capacity and act as an electron acceptor to promote the charge carrier separation, while Ce served as an electron/hole mediator. Thus, the combined effects of GO sheets and Ce ion contributed to the improved photoactivity of Ce- ZrO_2 -GO nanocomposite with regards to visible light absorption and electron transfer. Since $\text{O}_2^{\cdot-}$ and HO^{\cdot} played a key influence on the degradation of Ce- ZrO_2 -GO nanocomposite, the major routes in the photodegradation of EY dye

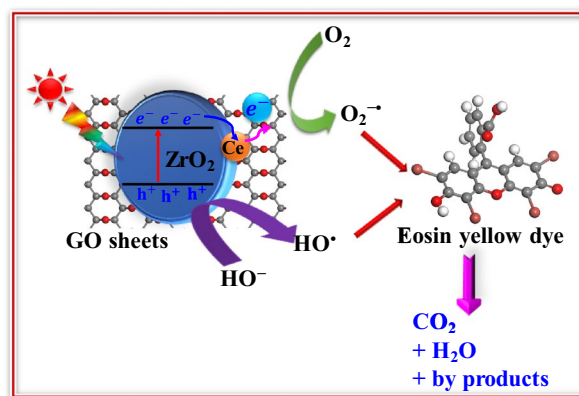
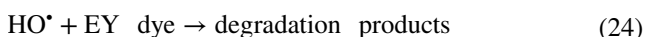
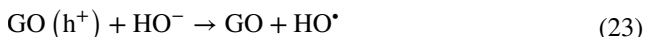
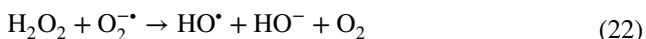
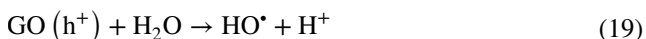
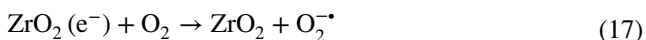
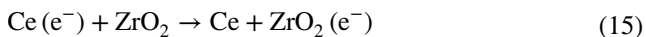
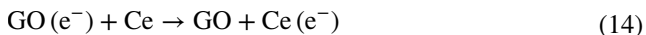


Fig. 12 Schematic illustration of the photocatalytic mechanism of Ce- ZrO_2 -GO nanocomposite under simulated visible light irradiation

mechanism under solar light irradiation were discussed, as given in Eqs. (13)–(24).



The electrons and holes accumulated on the CB and VB of GO sheets and ZrO₂ could reduce O₂ to O₂^{-•} and HO⁻ to HO[•], respectively. Afterwards, the O₂^{-•} radical anion could combine with the H⁺ to generate additional HO[•] radical. Therefore, aqueous EY dye solution could be readily adsorbed onto the surface of Ce–ZrO₂–GO because of the large surface area and then attacked by the reactive species to successfully photodegraded into CO₂, H₂O and other by products. Therefore, the improved photoactivity was ascribed to the improvement of direct semiconductor photoexcitation. The HO[•] radical is very non-selective in nature and rapidly reacts with numerous organic species with relatively higher rate constants between 10⁸ and 10¹⁰ M⁻¹ s⁻¹, which result in the formation of degradation products such as water, carbon dioxide and inorganic ions and/or biodegradable compounds [84, 85]. According to previous studies, the HO[•] radical can oxidise EY to environmentally benign products, such as water, carbon dioxide and inorganic salts, such as bromide ions [86]. Therefore, in this study, HO[•] radical participates as an active oxidizing species in the degradation of eosin yellow into water, carbon dioxide and inorganic salts, such as bromide ions, as the rate of degradation was appreciably reduced in the presence of hydroxyl radical scavenger.

4 Conclusion

In this study, the co-precipitation technique was employed to synthesise a nanostructure made up of Ce-doped–ZrO₂ anchored on graphene oxide. The photocatalytic activity of Ce–ZrO₂–GO nanocomposite was assessed by the photodegradation of EY dye under solar light irradiation. The interfacial charge migration, electronic structure, orbital composition, and the mechanism of the excellent visible light photocatalytic stability and activity was examined in the novel Ce–ZrO₂–GO nanocomposite using a hybrid DFT calculation. The EY dye photodegradation results showed that the Ce–ZrO₂–GO nanocomposite showed an enhanced activity and stability compared to pure ZrO₂. The optimum concentration of Ce ion in the nanocomposite was found to be 0.3%, beyond which the performance reduces. This was because of the improved adsorption of EY dye on its surface, narrow bandgap energy, an increased lifetime of charge carriers, enhanced visible light absorption and high surface area. The linear nature of the kinetics curves indicated that the photodegradation was a pseudo-first-order kinetics for the EY dye. Moreover, a 76% decrease in TOC was observed in the photocatalytic process and a high photodegradation efficiency was achieved after five cycles with remarkable stability. Superoxide radical anion and hydroxyl radicals were the key active species involved in the photodegradation of EY dye using Ce–ZrO₂–GO (0.3% Ce) nanocomposite. We showed that the HOL of Ce–ZrO₂–GO nanocomposite was dominated by ZrO₂ through the first-principles study and therefore, after contact, the ZrO₂ possessed a negative charge to induce a higher electrostatic interaction with GO sheets. Our calculations showed that Ce ions serve as an acceptor and a donor to the photogenerated electrons, which led to electron-rich surface. This study not only revealed that Ce–ZrO₂–GO nanocomposite could be a potential photocatalyst for photodegradation EY dye with a high stability and activity, but also offers a theoretical reference, and the role of GO and Ce ions in the nanocomposite can offer new insights in designing low-cost and highly efficient ZrO₂-based photocatalyst materials for applications in environmental remediation.

Acknowledgements The authors would like to acknowledge the financial contributions from the Faculty of Science: University of Johannesburg–South Africa, Centre for Nanomaterials and Science Research, Department of Applied Chemistry and the National Research Foundation (TTK14052167682). The authors are also grateful to the Centre for High Performance Computing (CHPC), Cape Town for access to their computational resources.

Compliance with Ethical Standards

Conflict of interest There are no conflicts to declare.

References

- Santhosh C, Velmurugan V, Jacob G, Jeong SK, Grace AN, Bhatnagar A (2016) Role of nanomaterials in water treatment applications: a review. *Chem Eng J* 306:1116–1137
- Liu B, Hu J, Foord JS (2011) Electrochemical deposition of zirconia films on diamond electrodes. *Electrochem Solid-State Lett* 14(2):D20–D22
- Raghu S, Basha CA (2007) Chemical or electrochemical techniques, followed by ion exchange, for recycle of textile dye wastewater. *J Hazard Mater* 149(2):324–330
- Zhang N, Yang M-Q, Liu S, Sun Y, Xu Y-J (2015) Waltzing with the versatile platform of graphene to synthesize composite photocatalysts. *Chem Rev* 115(18):10307–10377
- Chowdhury PR, Bhattacharyya KG (2015) Ni/Ti layered double hydroxide: synthesis, characterization and application as a photocatalyst for visible light degradation of aqueous methylene blue. *Dalton Trans* 44(15):6809–6824
- Ma R, Islam MJ, Reddy DA, Kim TK (2016) Transformation of CeO₂ into a mixed phase CeO₂/Ce₂O₃ nanohybrid by liquid phase pulsed laser ablation for enhanced photocatalytic activity through Z-scheme pattern. *Ceram Int* 42(16):18495–18502
- Islam MJ, Reddy DA, Ma R, Kim Y, Kim TK (2016) Reduced-graphene-oxide-wrapped BiOI-AgI heterostructured nanocomposite as a high-performance photocatalyst for dye degradation under solar light irradiation. *Solid State Sci* 61:32–39
- Islam MJ, Kim HK, Reddy DA, Kim Y, Ma R, Baek H, Kim J, Kim TK (2017) Hierarchical BiOI nanostructures supported on a metal organic framework as efficient photocatalysts for degradation of organic pollutants in water. *Dalton Trans* 46(18):6013–6023
- Samson K, Sliwa M, Socha RP, Góra-Marek K, Mucha D, Rutkowska-Zbik D, Paul J, Ruggiero-Mikołajczyk M, Grabowski R, Słoczyński J (2014) Influence of ZrO₂ structure and copper electronic state on activity of Cu/ZrO₂ catalysts in methanol synthesis from CO₂. *ACS Catal* 4(10):3730–3741
- Bautista P, Faraldos M, Yates M, Bahamonde A (2007) Influence of sulphate doping on Pd/zirconia based catalysts for the selective catalytic reduction of nitrogen oxides with methane. *Appl Catal B* 71(3–4):254–261
- Droushiotis N, Doraswami U, Kanawka K, Kelsall G, Li K (2009) Characterization of NiO–yttria stabilised zirconia (YSZ) hollow fibres for use as SOFC anodes. *Solid State Ionics* 180(17–19):1091–1099
- Chakravarty R, Shukla R, Ram R, Tyagi AK, Dash A, Venkatesh M (2010) Practicality of tetragonal nano-zirconia as a prospective sorbent in the preparation of 99 Mo/99 m Tc generator for biomedical applications. *Chromatographia* 72(9–10):875–884
- Ardiyanti A, Gutierrez A, Honkela M, Krause A, Heeres H (2011) Hydrotreatment of wood-based pyrolysis oil using zirconia-supported mono- and bimetallic (Pt, Pd, Rh) catalysts. *Appl Catal. A* 407(1–2):56–66
- Sadiq M, Ilyas M, Alam S (2012) Investigating the catalytic activity of monoclinic zirconia; oxidation of benzyl alcohol in aqueous medium at mild conditions. *Tenside Surfactants Deterg* 49(1):37–42
- Garcia JC, Scolfaro L, Lino A, Freire V, Farias G, Silva C, Alves HL, Rodrigues S, da Silva Jr E (2006) Structural, electronic, and optical properties of ZrO₂ from *ab initio* calculations. *J Appl Phys* 100(10):104103
- Hou W, Cronin SB (2013) A review of surface plasmon resonance-enhanced photocatalysis. *Adv Funct Mater* 23(13):1612–1619
- Sun M, Zhao Q, Du C, Liu Z (2015) Enhanced visible light photocatalytic activity in BiOCl/SnO₂: heterojunction of two wide band-gap semiconductors. *RSC Adv* 5(29):22740–22752
- Sun X-F, Qin J, Xia P-F, Guo B-B, Yang C-M, Song C, Wang S-G (2015) Graphene oxide–silver nanoparticle membrane for biofouling control and water purification. *Chem Eng J* 281:53–59
- Oppong SO, Anku WW, Shukla SK, Govender PP (2017) Synthesis and characterisation of neodymium doped-zinc oxide–graphene oxide nanocomposite as a highly efficient photocatalyst for enhanced degradation of indigo carmine in water under simulated solar light. *Res Chem Intermed* 43(1):481–501
- Nair AK, JagadeeshBabu P (2017) TiO₂ nanosheet-graphene oxide based photocatalytic hierarchical membrane for water purification. *Surf Coat Technol* 320:259–262
- El-Shafai NM, El-Khouly ME, El-Kemary M, Ramadan MS, Masoud MS (2018) Graphene oxide–metal oxide nanocomposites: fabrication, characterization and removal of cationic rhodamine B dye. *RSC Adv* 8(24):13323–13332
- Lu J, Zang J, Shan S, Huang H, Wang Y (2008) Synthesis and characterization of core–shell structural MWNT–zirconia nanocomposites. *Nano Lett* 8(11):4070–4074
- Kumar SV, Huang N, Yusoff N, Lim H (2013) High performance magnetically separable graphene/zinc oxide nanocomposite. *Mater Lett* 93:411–414
- Zalas M, Laniecki M (2005) Photocatalytic hydrogen generation over lanthanides-doped titania. *Sol Energy Mater Sol Cells* 89(2–3):287–296
- Zhao Z, Liu Q (2008) Effects of lanthanide doping on electronic structures and optical properties of anatase TiO₂ from density functional theory calculations. *J Phys D* 41(8):085417
- Fu C, Li T, Qi J, Pan J, Chen S, Cheng C (2010) Theoretical study on the electronic and optical properties of Ce³⁺-doped TiO₂ photocatalysts. *Chem Phys Lett* 494(1–3):117–122
- Piña-Pérez Y, Tzompantzi-Morales F, Pérez-Hernández R, Arroyo-Murillo R, Acevedo-Peña P, Gómez-Romero R (2017) Photocatalytic activity of Al₂O₃ improved by the addition of Ce³⁺/Ce⁴⁺ synthesized by the sol-gel method. Photodegradation of phenolic compounds using UV light. *Fuel* 198:11–21
- Xie Y, Yuan C (2003) Visible-light responsive cerium ion modified titania sol and nanocrystallites for X-3B dye photodegradation. *Appl Catal B* 46(2):251–259
- Oppong SO-B, Opoku F, Govender PP (2019) Tuning the electronic and structural properties of Gd-TiO₂-GO nanocomposites for enhancing photodegradation of IC dye: The role of Gd³⁺ ion. *Appl Catal B* 243:106–120
- Woan K, Pyrgiotakis G, Sigmund W (2009) Photocatalytic carbon-nanotube–TiO₂ composites. *Adv Mater* 21(21):2233–2239
- Kumaran SM, Gopalakrishnan R (2012) Structural, optical and photoluminescence properties of Zn_{1-x}Ce_xO (x = 0, 0.05 and 0.1) nanoparticles by sol–gel method annealed under Ar atmosphere. *J Sol-Gel Sci Technol* 62(2):193–200
- Clark SJ, Segall MD, Pickard CJ, Hasnip PJ, Probert MI, Refson K, Payne MC (2005) First principles methods using CASTEP. *Z Kristallogr Cryst Mater* 220(5/6):567–570
- Materials Studio Simulation Environment (2016) Release 2016. Accelrys Software Inc, San Diego
- Pfrommer BG, Côté M, Louie SG, Cohen ML (1997) Relaxation of crystals with the Quasi-Newton method. *J Comput Phys* 131(1):233–240
- Perdew JP, Burke K, Ernzerhof M (1996) Generalized gradient approximation made simple. *Phys Rev Lett* 77(18):3865–3868
- Vanderbilt D (1990) Soft self-consistent pseudopotentials in a generalized eigenvalue formalism. *Phys Rev B* 41(11):7892–7895
- Heyd J, Scuseria GE, Ernzerhof M (2003) Hybrid functionals based on a screened Coulomb potential. *J Chem Phys* 118(18):8207–8215
- Perdew JP (1986) Density functional theory and the band gap problem. *Int J Quantum Chem* 30(3):451–451

39. Monkhorst HJ, Pack JD (1976) Special points for Brillouin-zone integrations. *Phys Rev B* 13(12):5188–5192
40. Heshmatpour F, Aghakhanpour RB (2012) Synthesis and characterization of superfine pure tetragonal nanocrystalline sulfated zirconia powder by a non-alkoxide sol–gel route. *Adv Powder Technol* 23(1):80–87
41. Srinivasan R, De Angelis RJ, Ice G, Davis BH (1991) Identification of tetragonal and cubic structures of zirconia using synchrotron x-radiation source. *J Mater Res* 6(6):1287–1292
42. Shukla S, Seal S, Vij R, Bandyopadhyay S, Rahman Z (2002) Effect of nanocrystallite morphology on the metastable tetragonal phase stabilization in zirconia. *Nano Lett* 2(9):989–993
43. Marcano DC, Kosynkin DV, Berlin JM, Sinitskii A, Sun Z, Slesarev A, Alemany LB, Lu W, Tour JM (2010) Improved synthesis of graphene oxide. *ACS Nano* 4(8):4806–4814
44. Pawar RC, Khare V, Lee CS (2014) Hybrid photocatalysts using graphitic carbon nitride/cadmium sulfide/reduced graphene oxide (gC₃N₄/CdS/RGO) for superior photodegradation of organic pollutants under UV and visible light. *Dalton Trans* 43(33):12514–12527
45. Charanpahari A, Ghugal SG, Umare SS, Sasikala R (2015) Mineralization of malachite green dye over visible light responsive bismuth doped TiO₂–ZrO₂ ferromagnetic nanocomposites. *New J Chem* 39(5):3629–3638
46. Zhang Q, Zhang Y, Li H, Gao C, Zhao Y (2013) Heterogeneous CaO–ZrO₂ acid-base bifunctional catalysts for vapor-phase selective dehydration of 1, 4-butanediol to 3-buten-1-ol. *Appl Catal A* 466:233–239
47. Teymourian H, Salimi A, Firoozi S, Korani A, Soltanian S (2014) One-pot hydrothermal synthesis of zirconium dioxide nanoparticles decorated reduced graphene oxide composite as high performance electrochemical sensing and biosensing platform. *Electrochim Acta* 143:196–206
48. Yu X, Liu J, Yu Y, Zuo S, Li B (2014) Preparation and visible light photocatalytic activity of carbon quantum dots/TiO₂ nanosheet composites. *Carbon* 68:718–724
49. Luo D, Zhang G, Liu J, Sun X (2011) Evaluation criteria for reduced graphene oxide. *J Phys Chem C* 115(23):11327–11335
50. Panigrahy B, Srivastava S (2016) Minuscule weight percent of graphene oxide and reduced graphene oxide modified Ag₃PO₄: new insight into improved photocatalytic activity. *New J Chem* 40(4):3370–3384
51. Gurushantha K, Anantharaju K, Renuka L, Sharma S, Nagaswarupa H, Prashantha S, Vidya Y, Nagabhushana H (2017) New green synthesized reduced graphene oxide–ZrO₂ composite as high performance photocatalyst under sunlight. *RSC Adv* 7(21):12690–12703
52. An M, Li L, Tian Y, Yu H, Zhou Q (2018) The three-dimensional ordered macroporous structure of the Pt/TiO₂–ZrO₂ composite enhanced its photocatalytic performance for the photodegradation and photolysis of water. *RSC Adv* 8(34):18870–18879
53. Coulter JB, Birnie DP III (2018) Assessing Tauc plot slope quantification: ZnO thin films as a model system. *Phys Status Solidi b* 255(3):1700393
54. Yu Y, Jimmy CY, Chan C-Y, Che Y-K, Zhao J-C, Ding L, Ge W-K, Wong P-K (2005) Enhancement of adsorption and photocatalytic activity of TiO₂ by using carbon nanotubes for the treatment of azo dye. *Appl Catal B* 61(1–2):1–11
55. Singh BR, Shoeb M, Khan W, Naqvi AH (2015) Synthesis of graphene/zirconium oxide nanocomposite photocatalyst for the removal of rhodamine B dye from aqueous environment. *J Alloys Compd* 651:598–607
56. Zhang X, Guo T, Wang X, Wang Y, Fan C, Zhang H (2014) Facile composition-controlled preparation and photocatalytic application of BiOCl/Bi₂O₂CO₃ nanosheets. *Appl Catal B* 150:486–495
57. Wang LS, Xiao MW, Huang XJ, Wu YD (2009) Synthesis, characterization, and photocatalytic activities of titanate nanotubes surface-decorated by zinc oxide nanoparticles. *J Hazard Mater* 161(1):49–54
58. Jiang L, Fu H, Wang B (2006) Effects of Sn dopant on the photoinduced charge property and photocatalytic activity of TiO₂ nanoparticles. *Appl Catal B* 62(3):282–291
59. Xin B, Jing L, Ren Z, Wang B, Fu H (2005) Effects of simultaneously doped and deposited Ag on the photocatalytic activity and surface states of TiO₂. *J Phys Chem B* 109(7):2805–2809
60. Khanchandani S, Kundu S, Patra A, Ganguli AK (2013) Band gap tuning of ZnO/In₂S₃ core/shell nanorod arrays for enhanced visible-light-driven photocatalysis. *J Phys Chem C* 117(11):5558–5567
61. Hu Y, Qian H, Liu Y, Du G, Zhang F, Wang L, Hu X (2011) A microwave-assisted rapid route to synthesize ZnO/ZnS core-shell nanostructures via controllable surface sulfidation of ZnO nanorods. *CrystEngComm* 13(10):3438–3443
62. Tan C, Zhu G, Hojamberdiev M, Okada K, Liang J, Luo X, Liu P, Liu Y (2014) Co₃O₄ nanoparticles-loaded BiOCl nanoplates with the dominant {001} facets: efficient photodegradation of organic dyes under visible light. *Appl Catal B* 152:425–436
63. Jia W, Jia B, Qu F, Wu X (2013) Towards a highly efficient simulated sunlight driven photocatalyst: a case of heterostructured ZnO/ZnS hybrid structure. *Dalton Trans* 42(39):14178–14187
64. Feng Y, Feng N, Wei Y, Zhang G (2014) An in situ gelatin-assisted hydrothermal synthesis of ZnO–reduced graphene oxide composites with enhanced photocatalytic performance under ultraviolet and visible light. *RSC Adv* 4(16):7933–7943
65. Palominos R, Freer J, Mondaca M, Mansilla H (2008) Evidence for hole participation during the photocatalytic oxidation of the antibiotic flumequine. *J Photochem Photobiol A* 193(2–3):139–145
66. Sadakane M, Sasaki K, Kunioku H, Ohtani B, Ueda W, Abe R (2008) Preparation of nano-structured crystalline tungsten (VI) oxide and enhanced photocatalytic activity for decomposition of organic compounds under visible light irradiation. *Chem Commun*(48):6552–6554
67. Charanpahari A, Umare S, Sasikala R (2013) Effect of Ce, N and S multi-doping on the photocatalytic activity of TiO₂. *Appl Surf Sci* 282:408–414
68. Zhang F, Yediler A, Liang X (2007) Decomposition pathways and reaction intermediate formation of the purified, hydrolyzed azo reactive dye CI Reactive Red 120 during ozonation. *Chemosphere* 67(4):712–717
69. Tian X, Xu T, Wang Y, Meng S (2017) Hierarchical h-, m- and n-BiPO₄ microspheres: facile synthesis and application in the photocatalytic decomposition of refractory phenols and benzene. *RSC Adv* 7(58):36705–36713
70. Yang H, Li J, Yu L, Huang B, Ma Y, Dai Y (2018) A theoretical study on the electronic properties of in-plane CdS/ZnSe heterostructures: type-II band alignment for water splitting. *J Mater Chem A* 6(9):4161–4166
71. Opoku F, Govender KK, van Sittert CGCE, Govender PP (2018) Tuning the electronic structures, work functions, optical property and stability of bifunctional hybrid graphene oxide/V-doped NaNbO₃ type-II heterostructures: A promising photocatalyst for H₂ production. *Carbon* 136:187–195
72. Opoku F, Govender KK, van Sittert CGCE, Govender PP (2017) Understanding the mechanism of enhanced charge separation and visible light photocatalytic activity of modified wurtzite ZnO with nanoclusters of ZnS and graphene oxide: from a hybrid density functional study. *New J Chem* 41(16):8140–8155
73. Xu L, Huang W-Q, Wang L-L, Huang G-F, Peng P (2014) Mechanism of superior visible-light photocatalytic activity and stability

- of hybrid $\text{Ag}_3\text{PO}_4/\text{graphene}$ nanocomposite. *J Phys Chem C* 118(24):12972–12979
74. Türkmen A, Türkmen M, Tepe Y, Akyurt I (2005) Heavy metals in three commercially valuable fish species from Iskenderun Bay, Northern East Mediterranean Sea, Turkey. *Food Chem* 91(1):167–172
 75. Pan C, Li D, Ma X, Chen Y, Zhu Y (2011) Effects of distortion of PO_4 tetrahedron on the photocatalytic performances of BiPO_4 . *Catal Sci Technol* 1(8):1399–1405
 76. Hosseini Z, Taghavinia N, Sharifi N, Chavoshi M, Rahman M (2008) Fabrication of high conductivity TiO_2/Ag fibrous electrode by the electrophoretic deposition method. *J Phys Chem C* 112(47):18686–18689
 77. Leng W, Zhang Z, Zhang J, Cao C (2005) Investigation of the kinetics of a TiO_2 photoelectrocatalytic reaction involving charge transfer and recombination through surface states by electrochemical impedance spectroscopy. *J Phys Chem B* 109(31):15008–15023
 78. Mohaghegh N, Tasviri M, Rahimi E, Gholami MR (2015) A novel p–n junction $\text{Ag}_3\text{PO}_4/\text{BiPO}_4$ -based stabilized pickering emulsion for highly efficient photocatalysis. *RSC Adv* 5(17):12944–12955
 79. Duan Y, Fu N, Liu Q, Fang Y, Zhou X, Zhang J, Lin Y (2012) Sn-doped TiO_2 photoanode for dye-sensitized solar cells. *J Phys Chem C* 116(16):8888–8893
 80. Premkumar J (2004) Development of super-hydrophilicity on nitrogen-doped TiO_2 thin film surface by photoelectrochemical method under visible light. *Chem Mater* 16(21):3980–3981
 81. Yan X, Liu K, Shi W (2017) Facile synthesis of CdS/MnWO_4 heterojunction with enhanced visible-light-driven photocatalytic activity and mechanism investigation. *Colloids Surf Physicochem Eng Aspects* 520:138–145
 82. Xu Y, Schoonen MA (2000) The absolute energy positions of conduction and valence bands of selected semiconducting minerals. *Am Mineral* 85(3–4):543–556
 83. Ren F, Zhang J, Wang Y, Yao W (2016) A graphene-coupled Bi_2WO_6 nanocomposite with enhanced photocatalytic performance: a first-principles study. *Phys Chem Chem Phys* 18(20):14113–14121
 84. Sun L, Yao Y, Wang L, Mao Y, Huang Z, Yao D, Lu W, Chen W (2014) Efficient removal of dyes using activated carbon fibers coupled with 8-hydroxyquinoline ferric as a reusable Fenton-like catalyst. *Chem Eng J* 240:413–419
 85. Wang Y, Zhao G, Chai S, Zhao H, Wang Y (2013) Three-dimensional homogeneous ferrite-carbon aerogel: one pot fabrication and enhanced electro-Fenton reactivity. *ACS Appl Mater Interfaces* 5(3):842–852
 86. Anirudhan T, Rejeena S (2015) Photocatalytic degradation of eosin yellow using poly (pyrrole-co-aniline)-coated $\text{TiO}_2/\text{nanocellulose}$ composite under solar light irradiation. *Journal of Materials* 2015:1–11

Publisher's Note Springer Nature remains neutral with regard to jurisdictional claims in published maps and institutional affiliations.

Affiliations

Samuel Osei-Bonsu Oppong¹  · Francis Opoku¹  · William Wilson Anku¹  · Ephraim Muriithi Kiarri¹  · Penny Poomani Govender¹ 

✉ Francis Opoku
ofrancis2010@gmail.com

✉ Penny Poomani Govender
pennyg@uj.ac.za

¹ Department of Applied Chemistry, University of Johannesburg, P. O. Box 17011, Doornfontein Campus, Johannesburg 2028, South Africa